Ezrin Mediates Tethering of the γ-Aminobutyric Acid Transporter GAT1 to Actin Filaments Via a C-Terminal PDZ-Interacting Domain

P. I. Imoukhuede,[†‡] Fraser J. Moss,[‡] Darren J. Michael,[§] Robert H. Chow,[§] and Henry A. Lester[‡*]
[†]Bioengineering Division, [‡]Division of Biology, California Institute of Technology Pasadena, California 91125; and [§]Zilkha Neurogenetic Institute and Department of Physiology and Biophysics, Keck School of Medicine, University of Southern California, Los Angeles, California 90089

ABSTRACT A high density of neurotransmitter transporters on axons and presynaptic boutons is required for the efficient clearance of neurotransmitters from the synapse. Therefore, regulators of transporter trafficking (insertion, retrieval, and confinement) can play an important role in maintaining the transporter density necessary for effective function. We determined the interactions that confine GAT1 at the membrane by investigating the lateral mobility of GAT1-yellow fluorescent protein-8 (YFP8) expressed in neuroblastoma 2a cells. Through fluorescence recovery after photobleaching, we found that a significant fraction (~50%) of membrane-localized GAT1 is immobile on the time scale investigated (~150 s). The mobility of the transporter can be increased by depolymerizing actin or by interrupting the GAT1 postsynaptic density 95/Discs large/zona occludens 1 (PDZ)-interacting domain. Microtubule depolymerization, in contrast, does not affect GAT1 membrane mobility. We also identified ezrin as a major GAT1 adaptor to actin. Förster resonance energy transfer suggests that GAT1-YFP8 and cyan fluorescent (CFP) tagged ezrin (ezrin-CFP) exist within a complex that has a Förster resonance energy transfer efficiency of 19% ± 2%. This interaction can be diminished by disrupting the actin cytoskeleton. In addition, the disruption of actin results in a >3-fold increase in γ-aminobutyric acid uptake, apparently via a mechanism distinct from the PDZ-interacting protein. Our data reveal that actin confines GAT1 to the plasma membrane via ezrin, and this interaction is mediated through the PDZ-interacting domain of GAT1.

INTRODUCTION

The γ-aminobutyric acid (GABA) transporter GAT1 (1), a member of the SLC6 family of neurotransmitter transporters, is a 12-transmembrane domain protein that aids in terminating GABAergic synaptic signaling by transporting GABA into cells. GAT1 is the predominant GABA transporter in the brain, and is localized primarily on axons and presynaptic terminals of GABAergic inhibitory neurons; it is also expressed on astrocytes (2,3).

The uptake of each GABA molecule is coupled to the cotransport of two Na^+ ions and one Cl^- ion (4–6). The complete time for one transport cycle is ~100 ms, which is longer than the ~10-ms decay time constant of GABAergic postsynaptic currents (7). This implies that each transporter functions, at most, only once per synaptic event. To accommodate such functional constraints, a GAT1 density on the order of 1000 transporters/μm^2 is required (8). The actual measured density of GAT1 molecules on several membranes, including presynaptic boutons and axons, is 800–1300 transporters/μm^2 (8). Therefore, a high membrane density of GAT1 underlies the efficient clearance of GABA from the synaptic cleft and from nearby extrasynaptic compartments. Knowing that a high density of GAT1 on the membrane aids in clearance, one may ask how GAT1 trafficking is regulated, and how GAT1 is restricted among membrane compartments.

Some aspects of GAT1 trafficking have been studied, and GAT1 insertion and retrieval time constants of 1.1 and 0.7 min^{-1}, respectively, were obtained through biotinylation studies (9). Previous studies also revealed that that 30% of the total GAT1 protein exists within a pool of transporters adjacent to the membrane surface, acutely recycling in and out of the plasma membrane. One third of this pool (11% of the total GAT1) is resident in the plasma membrane in the basal state. The trafficking rates and high number of reserve GAT1 vesicles have the potential to affect GAT1 membrane density, and effectively increase GABA turnover.

We seek an understanding of the restriction of GAT1 mobility at the membrane and, by analogy, the restriction of other SLC6 family transporters. To this end, we applied fluorescence recovery after photobleaching (FRAP) to measure GAT1 movement at the plasma membrane. FRAP reveals both the time course and the mobile fraction for protein movement, which are governed by passive diffusion, by active processes, and by tethering within and near the plane of the membrane. Furthermore, lateral intramembrane diffusion is accepted as a form of protein trafficking, as revealed through recent work on postsynaptic receptors (the α-amino-3-hydroxy-5-methyl-4-isoxazolepropionic acid receptor [AMPAR], *N*-methyl-D-aspartic acid receptor [NMDAR], $GABA_A$ subunits, and glycine receptor) (9). Lateral movement of AMPAR is not only faster than trafficking by exocytosis, but it also accounts for a significant amount of AMPAR exchange in dendritic spines (10).

Membrane protein mobility can be reduced or restricted by linkage to the cytoskeleton (11,12). Therefore, we applied cytoskeleton disruptors to determine how interactions with actin and/or microtubules affect GAT1 mobility.

Membrane confinement often occurs through a cytoskeleton adaptor protein such as gephyrin, which serves as a scaffold

Submitted July 3, 2008, and accepted for publication November 25, 2008.

*Correspondence: lester@caltech.edu

Editor: Elliot L. Elson.

0006-3495/09/04/2949/12 $2.00

doi: 10.1016/j.bpj.2008.11.070

between the glycine receptor and microtubules (13), or ezrin, which tethers the cystic fibrosis transmembrane conductance regulator (CFTR) to actin (14). Therefore, we used Förster resonance energy transfer (FRET) to determine the proximity of an adaptor that may be involved in GAT1 restriction.

Altogether, the data reveal novel interactions between GAT1, ezrin, and the actin cytoskeleton, and these interactions require the GAT1 C-terminal postsynaptic density 95/Discs large/zona occludens 1 (PDZ)-interacting domain.

MATERIALS AND METHODS

Molecular biology

The green fluorescent protein (GFP) tagged mGAT1, $mGAT1_0$-GFP construct was previously described, and was termed mGAT1-GFP (8). In $GAT1_0$-GFP, added C-terminal residues (a linker followed by GFP) disrupt the endogenous PDZ-interaction domain of GAT1 (C-terminal sequence, $-AYI\text{-}CO_2^-$).

To generate the new fluorescent mutant, GAT1-YFP8, an intact PDZ-interaction motif is added at the C-terminus, following the yellow fluorescent protein (YFP) moiety. The wild-type mGAT1 open reading frame (ORF) is subcloned without its endogenous stop codon into the *Hin*dIII and *Eco*RI sites of the pcDNA3.1(+) expression vector (Invitrogen, Carlsbad, CA) multiple cloning site (MCS). The YFP (Clontech, Mountain View, CA) ORF into which we introduce the "monomeric" A206K mutation (15) is then inserted in the frame with the mGAT1 ORF at the *Not*I and *Xba*I sites of the pcDNA3.1(+) MCS. This results in a 12-amino-acid spacer between the end of the mGAT1 sequence and the beginning of the fluorophore. The method of Geiser et al. for the integration of polymerase chain reaction (PCR) fragments without the use of restriction enzymes was modified, to amplify the final eight codons of the hGAT1 C-terminal sequence from a source plasmid, using PfuTurbo C_x Hotstart polymerase (Stratagene, La Jolla, CA) with 5′ and 3′ extensions that corresponded to the 20–22 nucleotide regions that flank the intended site of insertion (16). The PCR product from this first PCR is integrated in the frame immediately after the YFP sequence, when used as the primers in a subsequent QuikChange II XL mutagenesis PCR reaction (100-ng product from the first PCR reaction: 20 ng destination plasmid; Stratagene).

The cyan and yellow fluorescent protein (CFP and YFP respectively) tagged ezrins, ezrin-CFP and YFP-ezrin, gifts from Dr. Forte and Lixin Zhu, were described by Zhu et al. (17). The YFP-syntaxin, a gift of Dr. W. Almers, was described by An and Almers (18).

Neuroblastoma-2a culture

Mouse neuroblastoma-2a (N2a) cells (ATCC, Manassas, VA) are grown at 37°C in 95% air, 5% CO_2, in N2a culture medium containing the following: 44.5% DMEM, 44.5% OptiMEM, 10% fetal bovine serum, and 1% penicillin/streptomycin (10,000 IU penicillin, 10,000 mg/mL streptomycin) (Invitrogen). After cells are grown to confluence, they are plated onto glass-bottom dishes at a density of 3.5×10^5 cells/dish. Before plating, 14-mm glass-bottom dishes (No. 0, Mattek, Ashland, MA) are coated with 0.05% polyethylimine (PEI) (Sigma, St. Louis, MO), pH 8.4, in borate buffer. The transfection of a total of 1 μg DNA per plate is performed 16–24 h later with Lipofectamine and Plus reagent (Invitrogen). The composition of the N2a imaging solution is (mM): 128 NaCl, 2.4 KCl, 25 HEPES, 1.2 $MgCl_2$, 3.2 $CaCl_2$, 1.2 KH_2PO_4, and 10 D-glucose (19).

Nocodazole treatment

Nocodazole (Sigma, St. Louis, MO) was dissolved in DMSO at a concentration of 5 mg/mL, and stored at −20°C. We added 10 μM nocodazole to the N2a culture medium, and cells were incubated for 16–24 h at 37°C. This concentration and incubation time followed established protocols for maximally depolymerizing microtubules (20–22). Before imaging, N2a culture medium was aspirated from cells, and cells were washed with imaging solution containing 10 μM nocodazole. Cells were allowed to equilibrate at room temperature for 30 min in the 10 μM nocodazole containing imaging solution.

Latrunculin B and cytochalasin D treatment

Latrunculin B (Sigma-Aldrich, St. Louis, MO) was dissolved in DMSO and stored at −20°C at a stock concentration of 2.5 mM. We added 5 μM latrunculin B to the imaging solution, which was warmed to 37°C before imaging. Cells were washed with latrunculin B solution, and incubated for 1 h in the solution before imaging. Cytochalasin D (Sigma, St. Louis, MO) was dissolved in DMSO and stored at −20°C at a stock concentration of 1 mg/mL. We added 1 μg/mL cytochalasin D to the imaging solution, and warmed it to 37°C. Cells were washed with the cytochalasin D solution, and were incubated in the solution for 1 h before imaging.

GABA uptake

Uptake assays were performed using 12-well plates 48 h after transfection as follows. Culture medium was aspirated, and cells were equilibrated for 10 min at room temperature in 1 mL Krebs-Ringer (KRH) buffer containing (in mM): 130 NaCl, 1.3 KCl, 2.2 $CaCl_2$, 1.2 $MgSO_4$, 1.2 KH_2PO_4, 10 D-glucose, and 10 HEPES, pH 7.4 (23). GABA uptake was initiated on aspiration of the KRH buffer and the addition of 500 μL 2.5 μM GABA and 25 nM [^{3}H]GABA in KRH at room temperature. Uptake was terminated by four rapid washes with KRH + GABA, using the same total GABA concentration as during the uptake step. Cells were lysed in 1 mL 2% SDS in phosphate-buffered saline (PBS). The [^{3}H]GABA accumulation was assayed by liquid scintillation spectrometry. Specific uptake was normalized to the total protein in each well, as determined using the BCA protein assay (Pierce; Rockford, IL). Actin disruption was performed by incubating cells with 5 μM latrunculin B for 1 h at 37°C before uptake. We also included 5 μM latrunculin B in both the KRH equilibration and the [^{3}H]GABA buffers.

Microtubule and nuclear labeling with TubulinTracker Green and Hoechst 33342

Microtubules were labeled according to the instructions of the supplier, using TubulinTracker Green reagent for live-cell tubulin labeling (Molecular Probes, Eugene, OR). Briefly, N2a nucleus was stained by the addition of 10 μg Hoechst 33342; microtubules were stained with TubulinTracker in Hanks' Balanced Salt Solution by incubating for 30 min at 37°C in a 5% CO_2 incubator. Cells were rinsed three times with warm imaging solution before imaging.

Actin labeling with rhodamine phalloidin

A 14-μM rhodamine-conjugated phalloidin (Cytoskeleton, Denver, CO) stock solution was prepared by dissolving the solid in methanol, and storing at −20°C. A fresh 4% solution of paraformaldehyde (Fluka, St. Louis, MO) at pH 7.4 was prepared. The medium was aspirated from the dishes, and cells were rinsed twice with 1 × PBS. Fixation and staining were performed by combining 4% paraformaldehyde, 0.1% Triton, and 2 units (5 μL) rhodamine phalloidin per dish (10 min, room temperature). After fixation, cells were washed twice with 1 × PBS.

Confocal imaging

All FRAP experiments were performed on an inverted Zeiss LSM 510 Meta (Carl Zeiss, Thornwood, NY), using a 63× Plan-Apochromat 1.4-NA oil-immersion objective. Fluorescence was collected using an HFT KP 700/514 nm beam-splitter (Carl Zeiss) and a 535–590-nm bandpass filter. The detector gain was modified to allow for near-saturating conditions for a given

region of interest (ROI). There was no change to gain settings for a given ROI. For footprint photobleach, a circular ROI was chosen with an area of $9.4 \pm 0.9\ \mu m^2$. For perimeter photobleach, a rectangular ROI was chosen with an area of $12.5 \pm 1.2\ \mu m^2$. The ROIs were photobleached at 25% laser transmission, using the 514-nm laser line of a 40-mW argon laser. Photobleaching was optimized to obtain ~80% photodestruction within the ROI. Prebleach and recovery images were collected at 0.25% laser transmission at 5-s intervals. Twelve-bit images were collected at a pixel resolution of 512×512. The pinhole diameter was set at 144 μm.

Dye-labeled N2a cells were imaged on an inverted Zeiss LSM 510 Meta at 12 bits and a 512×512 pixel resolution. Stack slices were at 100-nm intervals. Hoechst 33342 nuclear-labeled cells were imaged using a Plan-Apochromat 100× 1.4-NA oil-immersion objective, and were excited using a two-photon laser tuned to 700 nm at 2.5% laser transmission. Fluorescence was collected using the HFT KP 700/488 beam-splitter and FT 510 and BP 390-465 IR filters (Zeiss). Stack slices were at 100-nm intervals, and the pinhole diameter was maximal (693 μm). TubulinTracker Green-labeled N2a cells were imaged using a 100× 1.4-NA oil-immersion objective. Cells were excited with a 488-nm argon laser at 2.5% laser transmission. Fluorescence was collected with the HFT 488 beam-splitter and NFT 490 and BP 500-550 IR filters. Stack slices were at 100-nm intervals, and the pinhole diameter was 213 μm. Rhodamine phalloidin-labeled N2a cells were imaged with a Plan-Neuofluar 63× 1.25 oil-immersion objective. Cells were excited with a 543-nm helium neon laser at 7.75% laser transmission. Fluorescence was collected using a 488/543 beam-splitter and NFT 545 and bandpass 565–615 filters. The zoom was 2×, stack slices were at 550-nm intervals, and the pinhole was 121 μm.

The FRET experiments were performed on a Nikon C1si laser-scanning confocal microscope system (Nikon Instruments, Melville, NY), equipped with spectral imaging capabilities and a Prior (Rockland, ME) remote-focus stage, as described in Drenan et al. (24). Spectral FRET analysis was performed as described in Nashmi et al. (25). Data are reported as mean ± SE.

FRAP analysis

Raw data were processed using algorithms written in-house (MATLAB, The MathWorks, Natick, MA) to obtain the ratio fluorescence $= f(t) - b(t)/(f_{NB}(t) - b(t)) \times (f(t_o) - b(t_o))$. This expression was obtained by subtracting the background fluorescence, $b(t)$, correcting for the photobleaching that occurs during recovery scanning by obtaining the fluorescence in a region not bleached, f_{NB} (t), and normalizing to the prebleach fluorescence intensity $f(t_o)$. Normalized traces were averaged. Error bars are reported as the standard error of the mean. Normalized data were fitted to a double-exponential, five-parameter regression in SigmaPlot (Systat Software, Inc., San Jose, CA) of the form $F(t) = F_{bo} - ae^{-bt} - ce^{-dt}$, where F_{bo} is the initial value of fluorescence after photobleaching, and a, b, c, and d are constants obtained through fitting. The mobile fraction was determined by applying regression data to the equation $M_f = \frac{F_\infty - F_{bo}}{1 - F_{bo}}$, where M_f is the mobile fraction and F_∞ is the asymptote of the recovery curve. Values for $t_{\frac{1}{2}}$ were determined by applying regression data to the equations $F_h = \frac{F_\infty + F_{bo}}{2}$, $t_{\frac{1}{2}} = t_h - t_{bo}$, where F_h is the value for fluorescence when half the recovery has occurred, t_h is the corresponding time for F_h, t_{bo} is the time after photobleaching when the first recovery image is obtained, and $t_{\frac{1}{2}}$ is the halftime of equilibration (26).

Real-time quantitative reverse-transcription PCR

Total RNA was prepared using the RNeasy Plus Mini Kit (Qiagen, Valencia, CA). The RNA concentrations were quantified using the ND-1000 UV-Vis Spectrophotometer (Nanodrop Technologies, Wilmington, DE). The primer and probe sets for Pals1, ezrin, β-actin, and γ-actin were designed by the Roche Universal Probe Library (UPL) Assay Design Center (Roche Applied Science, Indianapolis, IN). Primer sets were obtained from Integrated DNA Technologies (Coralville, IA). Table 1 displays the primer and probe sets used for the real-time quantitative reverse-transcription PCR (qRT-PCR) analysis of each gene in the N2a cells. One-step qRT-PCR was performed using a hydrolysis probe mix, 96-well plates, and the LightCycler 480 RNA Master system (Roche Applied Science), according to the supplier's instructions. Briefly, samples along with serially diluted mRNA (1:50, 1:100, 1:1000, 1:5000, and 1:10,000) were added to adjacent wells of the plate, centrifuged for 2 min at $1500 \times g$, and loaded into the instrument. The one-step qRT-PCR was performed as follows: one cycle of reverse transcription at 61°C for 12 min; one cycle of denaturation at 95°C for 30 s; 45 cycles of amplification at 95°C for 10 s, 57°C for 30 s, and 72°C for 1 s; and one cycle of cooling at 50°C for 10 s. Serial dilutions of mRNA provided the standard curves needed to quantify relative mRNA concentrations.

Statistical analysis

Values are expressed as mean ± SE, unless otherwise noted, and $p < 0.05$ is considered statistically significant.

RESULTS

In this study, we used an optimized mouse GAT1 that was fused with YFP at the GAT1 C-terminus, followed by an additional eight residues that included a PDZ domain binding site. This construct, GAT1-YFP8, produces the same maximal GABA uptake and has the same GABA concentration dependence as the wild-type transporter (Fig. S1 in the Supporting Material). In addition, the N2a assay system is linear and nonsaturated (data not shown). We report elsewhere that the GAT1-YFP8 transporter dimerizes correctly, and is correctly trafficked to the plasma membrane. Furthermore, the surface/cytoplasmic expression ratio is sensitive, as in neurons, to disruption of the PDZ interaction motif at the C-terminus of GAT1. We therefore think that this assay system closely resembles the native GAT1 transporter, expressed in the GABAergic neurons that constitute the native environment of GAT1.

TABLE 1 Primers and UPL probes used in qRT-PCR analysis of Pals1, ezrin, β-actin, and γ-actin expression in N2a cells

Protein (gene accession no.)	Primer sequences		Roche UPL No.
	Forward (5′ → 3′)	Reverse (5′ → 3′)	
Pals1 (NM_019579.1)	TGATTCCTAGTCAACAGATCAAGC	GTCAAAATGAGCTTTCACATGG	51
Ezrin (NM_009510.2)	AGCCGAATAGCCGAGGAC	GTCACCCGGACGTTGATT	21
β-actin (NM_007393.1)	CTAAGGCCAACCGTGAAAAG	ACCAGAGGCATACAGGGACA	64
γ-actin (NM_009609.2)	GAGCACGCTGTAGATGAGAAAG	GATCACTCAGTGGTGCTCACA	64

Whole-footprint photobleach reveals lateral mobility

The question often arises whether FRAP actually detects lateral mobility, or whether it detects the fusion of vesicles that are actively trafficking protein onto the membrane. To address this question, we performed "whole footprint" FRAP. Fig. 1 *A* gives prebleach, postbleach, and recovery images of a whole-footprint FRAP experiment. The postbleach image shows that >90% of the footprint surface area is photobleached, and includes a line profile across the bleached region. The ends of the line overlap nonphotobleached regions. The kymograph in Fig. 1 *B* represents the line profile, as shown in Fig. 1 *A*, over time, and it shows that recovery occurs from regions not photobleached, with fluorophore entering from the edges. This qualitative analysis indicates that FRAP largely reveals the lateral mobility of GAT1. However, it is possible that the speckles that appear in the image after ~60 s represent some contribution from vesicle exocytosis (9). In separate experiments, we visualized and tracked individual vesicles containing GAT1; these will be reported in a future study.

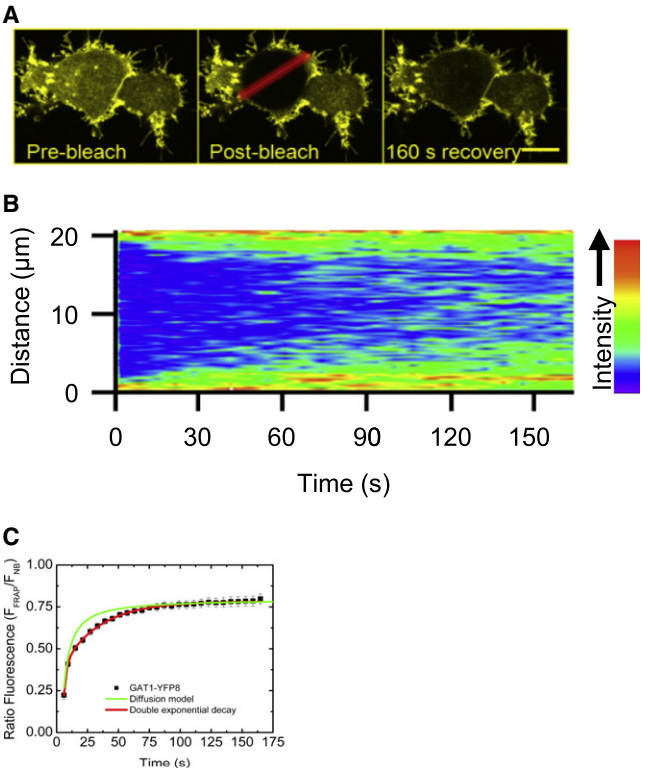

FIGURE 1 Whole-footprint photobleach reveals lateral mobility. (*A*) Confocal images of GAT1-YFP8 localized at the cell footprint show a prephotobleached and postphotobleached region of interest representing >90% of the footprint surface area. Scale bar, 10 μm. (*B*) The kymograph is obtained by measuring the intensity along the red line, which is a section of the photobleached region. The line profile is plotted over time. The intensity key shows that photobleached regions are represented by "cooler" colors, and increased fluorescence is represented by "hotter" colors. (*C*) Diffusion model is simulated using the Axelrod-Sprague pure-diffusion model and data from GAT1-YFP8 footprint FRAP recovery. The GAT1-YFP8 recovery curve is not well-fitted by the Axelrod-Sprague pure-diffusion model. The GAT1-YFP8 footprint FRAP recovery curve does fit a double-exponential decay equation, $F(t) = F_{bo} - ae^{-bt} - ce^{-dt}$, where a, b, c, and d = 3.3, 0.30, 0.45, and 0.033, respectively.

Fitting data to FRAP diffusion model

The diffusion model in Fig. 1 *C* is for a circular bleach spot, derived by Axelrod et al. (27), and modified by Sprague et al. (28) and Sprague and McNally (29). The model is as follows:

$$\frac{\partial f}{\partial t} = D_f \nabla^2 f$$

$$\tau_D = \frac{t_{\frac{1}{2}}}{\gamma} = \frac{\omega^2}{D_{eff}}$$

$$\sigma = 1 - A$$

$$F(t) = e^{-\frac{\tau_D}{2t}}\left[I_o\left(\frac{\tau_D}{2t}\right) + I_1\left(\frac{\tau_D}{2t}\right)\right] - \sigma$$

Based on the Axelrod-Sprague equation, γ is a constant equal to 0.88 for a circular beam with a Gaussian intensity profile, τ_D is the recovery time constant, ω is the radius of the bleach spot, D_{eff} is the effective diffusion coefficient, and A represents the recovery asymptote for GAT1-YFP8. Therefore, σ is a correction that allows the diffusion model to converge to the GAT1-YFP8 recovery asymptote. The Axelrod-Sprague equation does not accurately describe the behavior of GAT1-YFP8 recovery, suggesting that the mobility of the transporter is not governed by pure diffusion. In particular, the model exhibits sharp recovery at early time points. The recovery of GAT1-YFP8 is well-fitted as double-exponential decay (as described in Materials and Methods). Because the double-exponential fitting more accurately describes GAT1-YFP8 mobility on the time scale (~150 s) of these experiments, $t_{1/2}$ values are used in this study, rather than diffusion coefficients.

Comparing and quantifying GAT1 mobility

To give a context to GAT1 mobility, we compare it with minimally mobile and maximally mobile proteins, represented respectively by soluble YFP and by YFP-syntaxin1A, a t-SNARE membrane protein (Fig. 2, *A* and *B*). Footprint photobleach is chosen, because YFP is not a membrane protein, and cannot be meaningfully analyzed with a perimeter photobleach. However, its mobility near the membrane can be obtained by focusing near the coverslip. Within the first seconds of detection, there is steep, unresolved recovery of YFP to ~60% of its prebleach intensity; this limits the quantitative analysis of the YFP mobile fraction (Fig. 2 *C*). However, a qualitative observation of Fig. 2 *C* shows that the YFP recovery asymptote is greater than that of GAT1-YFP8, and by extrapolating the initial YFP photobleach to 20% (GAT1-YFP8 F_{bo}), we infer that YFP has a higher mobile fraction than GAT1-YFP8. As shown in Fig. 2 *B*,

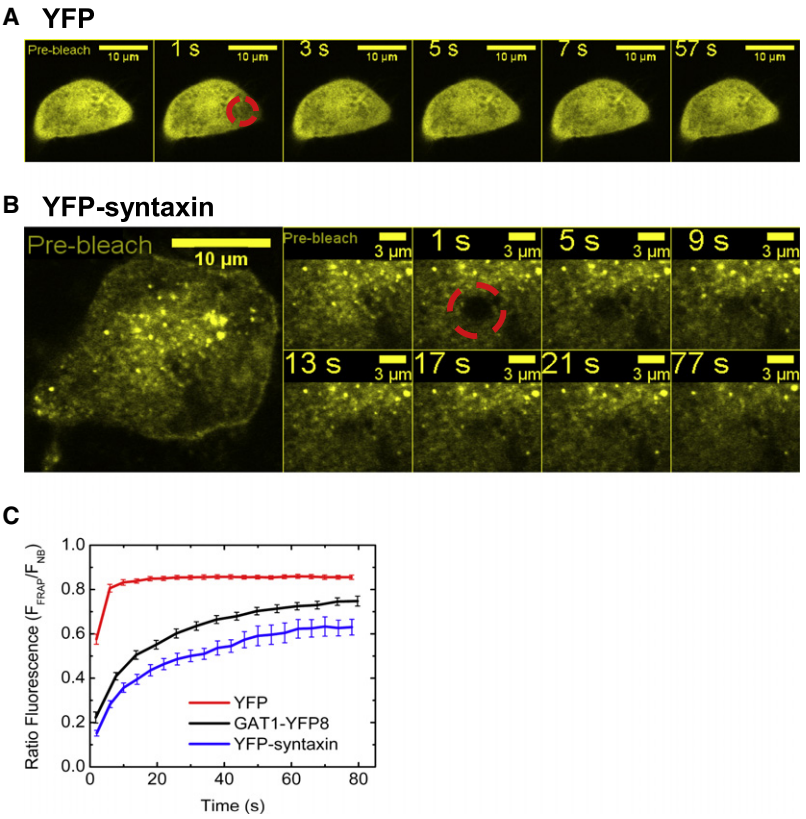

FIGURE 2 Comparing GAT1 mobility with cytosolic and membrane inserted proteins. Footprint FRAP was performed on GAT1-YFP8 (not shown), (*A*) YFP, and (*B*) YFP-syntaxin. (*C*) Recovery curves show that YFP, a soluble cytosolic protein, has a faster recovery than either of the membrane proteins. The initial YFP recovery was faster than the resolution of detection. The membrane proteins GAT1-YFP8 and syntaxin-YFP recovered at similar rates.

and as previously reported, YFP-syntaxin clusters to form exocytosis docking sites at the membrane, so it is not expected to have high membrane mobility (30). YFP-syntaxin has a mobile fraction of 65%, comparable to the GAT1-YFP8 mobile fraction of 60% (Fig. 2 *C*).

Photobleach regions

Variations in imaging parameters, such as laser intensity, bleach size/shape, and pixel dwell time, can affect the results of quantitative photobleach experiments (31). To provide additional confirmation of the FRAP results, GAT1 experiments were performed by photobleaching the cell footprint and perimeter, and comparing the trends seen between these regions of interest (Fig. 3, *A* and *B*). The approximate size for footprint photobleach is a circle with an area of 8 μm^2 (Fig. 3 *A*). Perimeter photobleach is performed by focusing the laser on a plane vertically midway through the cell, and a rectangular section, including the cell membrane (with an area of 13 μm^2), is photobleached (Fig. 3 *B*). Perimeter photobleach recovery occurs in two dimensions, and the membrane fluorescence in the confocal slice is a line representation of this recovery. Footprint and perimeter photobleach revealed GAT1-YFP8 mobile fractions of ~60% and 50%, respectively (Fig. 3 *C*). These results suggest that 40–50% of GAT1-YFP8 is immobilized on the time scale (~150 s) of these experiments. Because a significant fraction of surface GAT1 is immobile, we explored the possibility of GAT1 tethering to the cytoskeleton.

GAT1 interacts with cytoskeleton via actin but not via microtubules

Fig. 4 *A* (*left*) displays microtubule distribution in an N2a cell labeled with TubulinTracker 488. Fig. 4 *A* (*right*) includes nuclear labeling with Hoechst 33342. Applying nocodazole for 16–24 h maximally disrupts microtubules (20) (Fig. 4 *B*). The FRAP traces show that nocodazole treatment has no significant effect on either the recovery time constant or the size of the mobile population (Fig. 4, *C* and *D*).

Rhodamine phalloidin labeling of actin filaments in N2a cells confirms the actin disruption (Fig. 4, *E* and *F*). Modest differences were evident between the untreated and the latrunculin B footprint photobleach traces, which translate to a 20% increase in the mobile fraction (Fig. 4, *G* and *I*). More pronounced differences in the untreated and latrunculin B perimeter photobleach traces reveal a 60% increase in the time constant for recovery, and a 20% increase in the mobile fraction (Fig. 4, *H–J*). Cytochalasin D, another actin disruptor, confirms the latrunculin B results, with an increased $t_{1/2}$ and an increased mobile fraction compared with the untreated samples (Fig. 4, *I* and *J*).

Disrupting PDZ binding increases GAT1 lateral mobility

Typically, actin binding occurs through an adaptor protein, or by an interaction with a scaffolding protein such as a PDZ protein (13,32–34). To determine whether PDZ

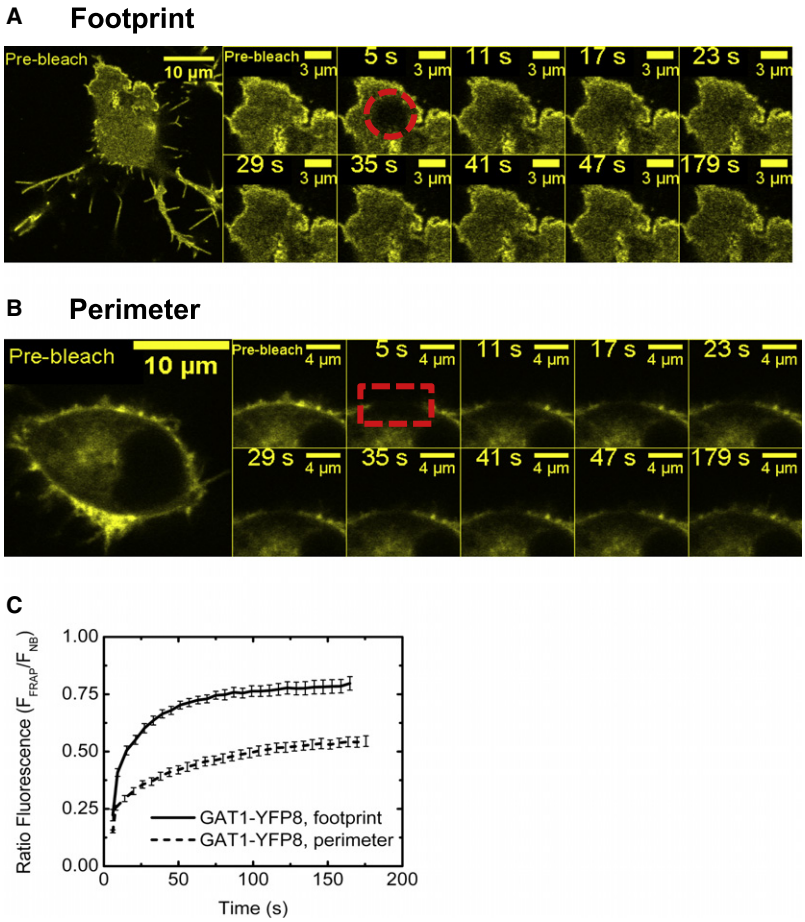

FIGURE 3 Photobleached regions. FRAP prebleach and postbleach images of N2a cells expressing GAT1-YFP8. (*A*) Photobleaching is confined to cell footprint within red circle (8 μm^2). Scale bar, 3 μm. (*B*) Photobleaching is confined to cell perimeter, within red rectangle (13 μm^2). Scale bar, 4 μm. (*C*) GAT1-YFP8 footprint photobleach gave a recovery $t_{1/2} = 10$ s, and a mobile fraction of 60%. GAT1-YFP8 perimeter photobleach gave a recovery $t_{1/2} = 20$ s, and a mobile fraction of 50%.

binding links GAT1 to the actin cytoskeleton, we performed quantitative photobleaching on $GAT1_0$-GFP, a fluorescent GAT1 that cannot interact with PDZ proteins. In $GAT1_0$-GFP, added C-terminal residues (a linker followed by GFP) interrupted the endogenous PDZ-interaction domain of GAT1 (C-terminal sequence, $-AYI\text{-}CO_2^-$). As a result, homozygous $GAT1_0$-GFP knock-in mice showed a 70% reduction in surface localization and synaptosomal GABA uptake (8). Fig. 5 *A* illustrates the difference between the two fluorescent GABA transporter constructs in this study: $GAT1_0$-GFP lacks an intact PDZ-interacting domain, whereas we inserted a PDZ-interaction domain to GAT1-YFP8, downstream of the YFP moiety.

FRAP was performed on N2a cells transfected with $GAT1_0$-GFP. The $GAT1_0$-GFP was 30–40% more mobile on the membrane than GAT1-YFP8, indicating that the PDZ interaction domain contributes to GAT1 immobilization (Fig. 5 *B*). Latrunculin B treatment shows that depolymerizing actin does not significantly affect the mobile fraction (Fig. 5 *B*). Because the PDZ-binding domain of $GAT1_0$-GFP was disrupted and this led to no interaction with actin, we conclude that a PDZ-interacting domain in GAT1 is necessary, either directly or indirectly, for GAT1-actin interactions.

Actin disruption increases GABA uptake

Disruption of actin increases Na^+-dependent GABA uptake in BGT1, a GABA transporter subtype that, like GAT1, is expressed in the central nervous system, but unlike GAT1, is also expressed in the kidney (35,36). To determine whether actin disruption can increase GABA uptake by GAT1, we performed GABA uptake on both actin-disrupted and nontreated cells. Actin disruption increased the GABA uptake of both GAT1-YFP8 and the poorly trafficking $GAT1_0$-GFP (Fig. 5 *C*). These statistically significant increases amounted to a 3.4-fold increase in GABA uptake by GAT1-YFP8, and a 3.1-fold increase in the much lower GABA uptake by $GAT1_0$-GFP. Both increases were relative to non-latrunculin B-treated controls.

Ezrin and Pals1 are expressed in N2a cells

The FRAP results indicate that GAT1 interacts with the cytoskeleton through the PDZ-binding motif. Another membrane protein with this type of interaction is the Na^+/H^+ exchanger isoform 3 (NHE3), which is restrained to actin through interactions with the PDZ protein, the Na^+-H^+ exchanger regulatory factor (NHERF), and the adaptor protein ezrin (37). To determine whether ezrin could link GAT1 to the

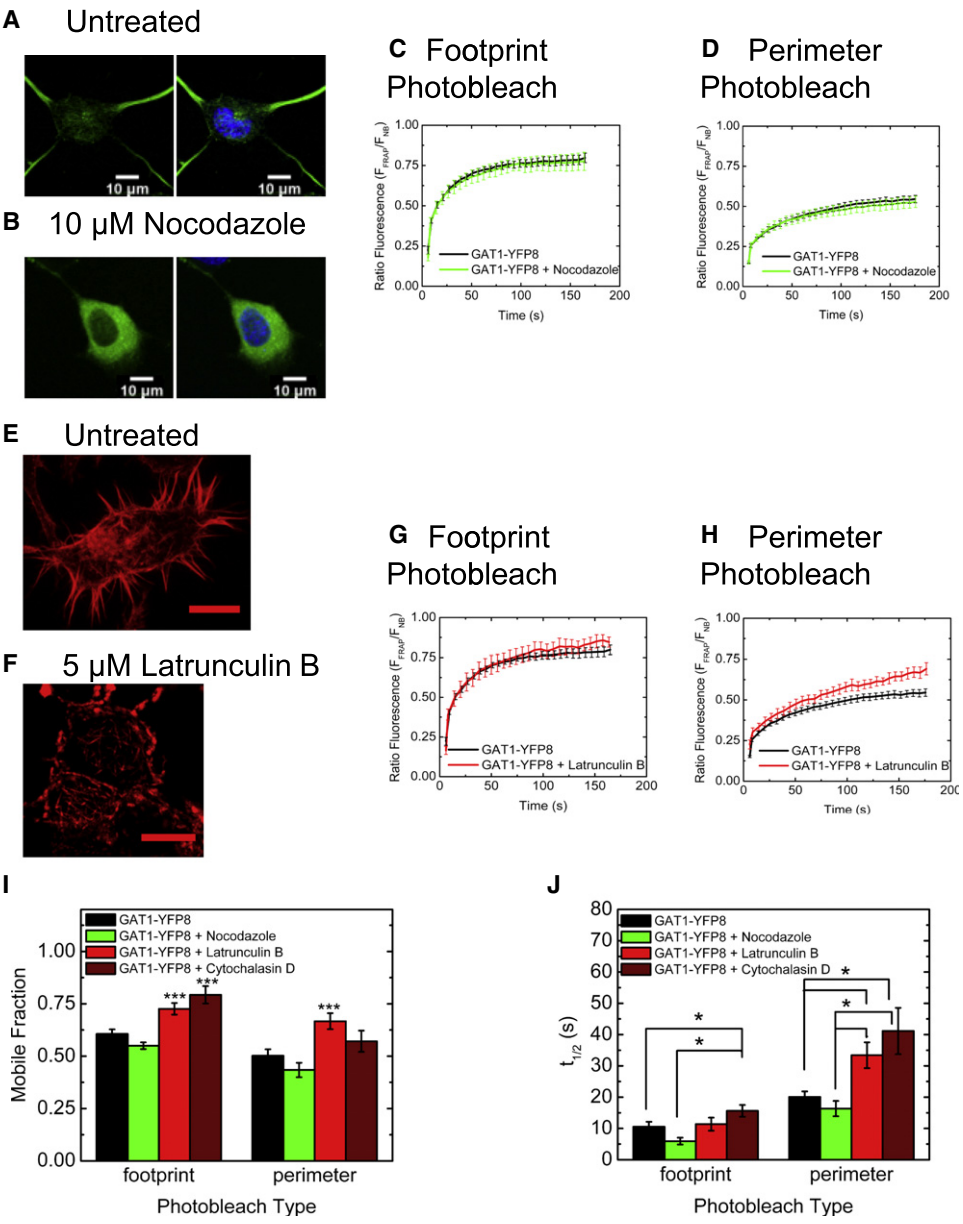

FIGURE 4 GAT1 associates with actin, but does not associate with microtubules. (*A*, *B*) Microtubules are visible after treatment with TubulinTracker 488. Right-hand panels display nuclear labeling with Hoechst 33342. (*B*) Microtubules are disrupted by treatment with 10 μM nocodazole. Scale bars, 10 μm. (*C*, *D*) Traces display GAT1-YFP8 fluorescence recovery in cells with and without intact microtubules. Cells are photobleached at the footprint (*C*) and at cell perimeter (*D*). (*E*, *F*) Actin is revealed after N2a cells are treated with rhodamine-conjugated phalloidin. (*F*) Actin filaments are disrupted by treatment with latrunculin B. Scale bars, 10 μm. Traces display GAT1-YFP8 fluorescence recovery in cells with and without an intact actin network. Fluorescence is photobleached at the cell footprint (*G*) and at the cell perimeter (*H*). (*I*) GAT1-YFP8 mobile fraction. Disrupting actin with 5 μM latrunculin B significantly increases the amount of freely diffusing GAT1 on the plasma membrane ($p < 0.001$, *t*-test). The addition of 1 μg/mL cytochalasin D, another actin depolymerizer, also significantly increases the mobile fraction when probed with footprint photobleach ($p < 0.001$, *t*-test). Depolymerizing microtubules with 10 μM nocodazole does not affect the mobile fraction of GAT1-YFP8. (*J*) GAT1-YFP8 time constant. Disrupting actin with cytochalasin D or latrunculin B increases the time for recovery with perimeter photobleach ($p < 0.05$, Mann-Whitney test). Cytochalasin D treatment also significantly increases the time constant for recovery with footprint photobleach ($p < 0.05$, Mann-Whitney test). Microtubule disruption does not significantly affect the time constant. GAT1-YFP8 footprint, n = 18; GAT1-YFP8 + nocodazole footprint, $n = 8$; GAT1-YFP8 + latrunculin B footprint, $n = 12$, GAT1-YFP8 + cytochalasin D footprint, $n = 10$; GAT1-YFP8 perimeter, $n = 12$; GAT1-YFP8 + nocodazole perimeter, $n = 9$; GAT1-YFP8 + latrunculin B perimeter, $n = 12$; GAT1-YFP8 + cytochalasin D perimeter, $n = 10$.

cytoskeleton, we performed qRT-PCR, testing for the expression of two genes: the PDZ protein known to interact with GAT1, Pals1 (38), and the linker molecule ezrin. The N2a cells expressed both ezrin and Pals1 mRNA at similar levels (Fig. 6 *A*). The mRNA expression was normalized to the β-actin control; γ-actin was also used as a control, with expression levels similar to those of β-actin (Fig. 6 *A*).

FRET suggests a GAT1-ezrin interaction

Figs. 6, *B–H*, display the results of FRET experiments that combined donor recovery after acceptor photobleach with spectral unmixing. After the photodestruction of GAT1-YFP8 with a 514-nm argon laser, there was a 23% increase in ezrin-CFP fluorescence (Fig. 6, *B* and *E*). This increase was seen most prominently along the cell membrane (Fig. 6 B). The FRET efficiency observed between GAT1-YFP8 and ezrin-CFP was 19% ± 2% (Fig. 6 *F*).

Inactive ezrin forms C-terminal to N-terminal dimers in the cytosol (17,39). Therefore, the previously studied FRET partners, ezrin-CFP/YFP-ezrin (17), were used as a positive control. As expected, ezrin-CFP and YFP-ezrin were localized in the cytosol, and exhibited a FRET efficiency of 20% ± 2% (Fig. 6, *D* and *F*).

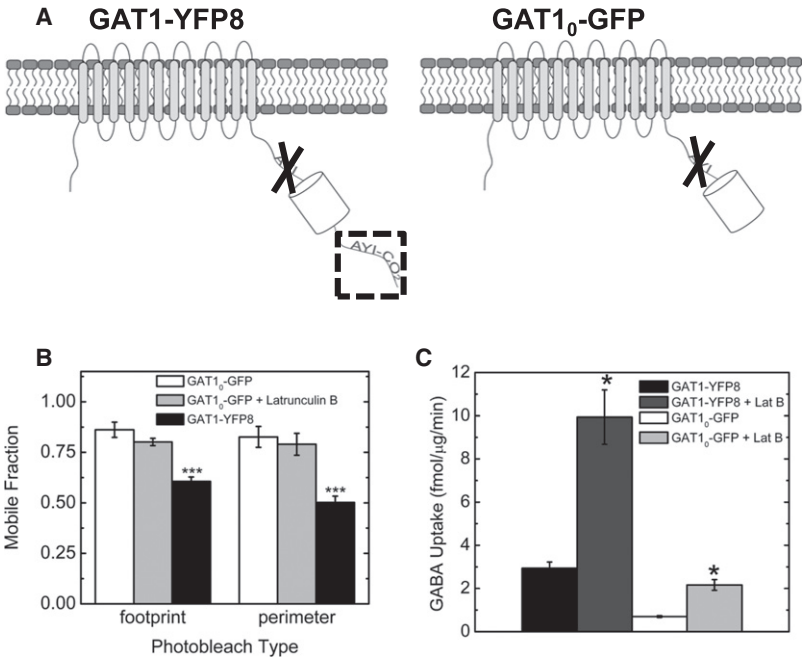

FIGURE 5 GAT1-YFP8 and GAT1$_0$-GFP schematics, FRAP, and GABA uptake. (*A*) Schematics of GAT1-YFP8 and GAT1$_0$-GFP. GAT1$_0$-GFP is mostly found in vesicles near the plasma membrane (8). This faulty trafficking arises because the addition of linker and GFP moiety interrupts the PDZ-binding motif. GAT1-YFP8 traffics properly due to the addition of eight amino acids after the fluorescent protein, the final three amino acids being a consensus PDZ-binding motif, AYI-CO_2^-. (*B*) GAT1$_0$-GFP has a higher mobile fraction than GAT1-YFP8 ($p < 0.05$, *t*-test). Disrupting actin does not significantly affect the mobile fraction of GAT1$_0$-GFP, compared with GAT1$_0$-GFP mobility in cells with intact actin. GAT1$_0$-GFP footprint, $n = 9$; GAT1$_0$-GFP + latrunculin B footprint, n = 9; GAT1$_0$-GFP perimeter, $n = 12$; GAT1$_0$-GFP + latrunculin B perimeter, $n = 10$. (*C*) Disrupting actin filaments through 1-h treatment with 5 μM latrunculin B significantly increases GABA uptake by GAT1-YFP8 and GAT1$_0$-GFP, relative to nontreated cells ($p < 0.001$, Mann-Whitney test).

Actin disruption diminishes GAT1-ezrin interaction

GAT1-YFP8 photodestruction resulted in little or no increase in ezrin-CFP fluorescence when actin was disrupted (Fig. 6, *C* and *E*). Latrunculin B exposure produced a FRET efficiency of 7% $\pm$ 5%, i.e., significantly lower than the FRET value for both untreated and ezrin-CFP/YFP-ezrin control samples (Fig. 6 *F*). These results indicate that actin depolymerization greatly destabilizes the interaction between GAT1 and ezrin.

There is no GAT1$_0$-ezrin interaction

If the interaction between GAT1 and ezrin requires a PDZ-binding motif, we expected to observe no such interaction between ezrin and a GAT1 molecule that lacks such a motif. GAT1$_0$-YFP provided an appropriate test. As expected, no detectable increase in ezrin-CFP fluorescence accompanied the photodestruction of GAT1$_0$-YFP (Fig. 6, *G* and *H*). This result supports the idea that the interaction between ezrin and GAT1 requires the binding motif.

DISCUSSION

This study establishes the role of lateral mobility in regulating GAT1 localization, by quantifying the mobility of GAT1 at the plasma membrane in an assay system resembling the native mouse neurons that express mGAT1. Previous studies on membrane proteins also used FRAP, the most appropriate quantitative method for measuring membrane protein mobility, in conjunction with manipulations of PDZ-interaction domains (40–43).

Our FRAP experiments show that ~50% of membrane-localized GAT1 molecules are mobile. Of the ~50% that are immobile, a fraction associates with the actin cytoskeleton. This conclusion is based on a significant increase in the mobile fraction of GAT1 in two experiments: 1), in cells treated with pharmacological agents known to disrupt actin filaments; and 2), in cells expressing a form of fluorescently tagged GAT1 with a disrupted PDZ-interaction domain. The magnitude of the increase in the mobile fraction of GAT1 was similar in both of these experiments. Moreover, the mobility of GAT1$_0$-GFP, which has a disrupted PDZ-interaction domain, could not be increased further by treating cells with an actin disruptor, more strongly implicating this domain in GAT1-actin interactions.

The PDZ-interacting domain of GAT1 plays an important role in tethering, and this fact indicates a link between GAT1 and actin. Most likely, this link is indirect, and is mediated by a PDZ protein and a linker protein. Ion channels that bind to PDZ proteins provide models for this interaction. PSD-95/SAP-90, a member of the membrane-associated guanylate kinase family of PDZ proteins, serves as a scaffold for the NMDA receptor, thereby clustering it on the postsynaptic membrane (44). This type of PDZ scaffolding also occurs through the action of two known PDZ domain-containing proteins (NHERF-1 and NHERF-2) on the CFTR (45). The CFTR is linked to the actin cytoskeleton through interactions between the PDZ domains of the proteins NHERF-1 and NHERF-2, and the actin binding protein, ezrin (14,40).

Biochemical investigations established interactions between GAT1 and the PDZ protein, Pals1 (38), and between Pals1 and the actin adaptor, ezrin (46). We showed via reverse transcription-PCR that Pals1 and ezrin are

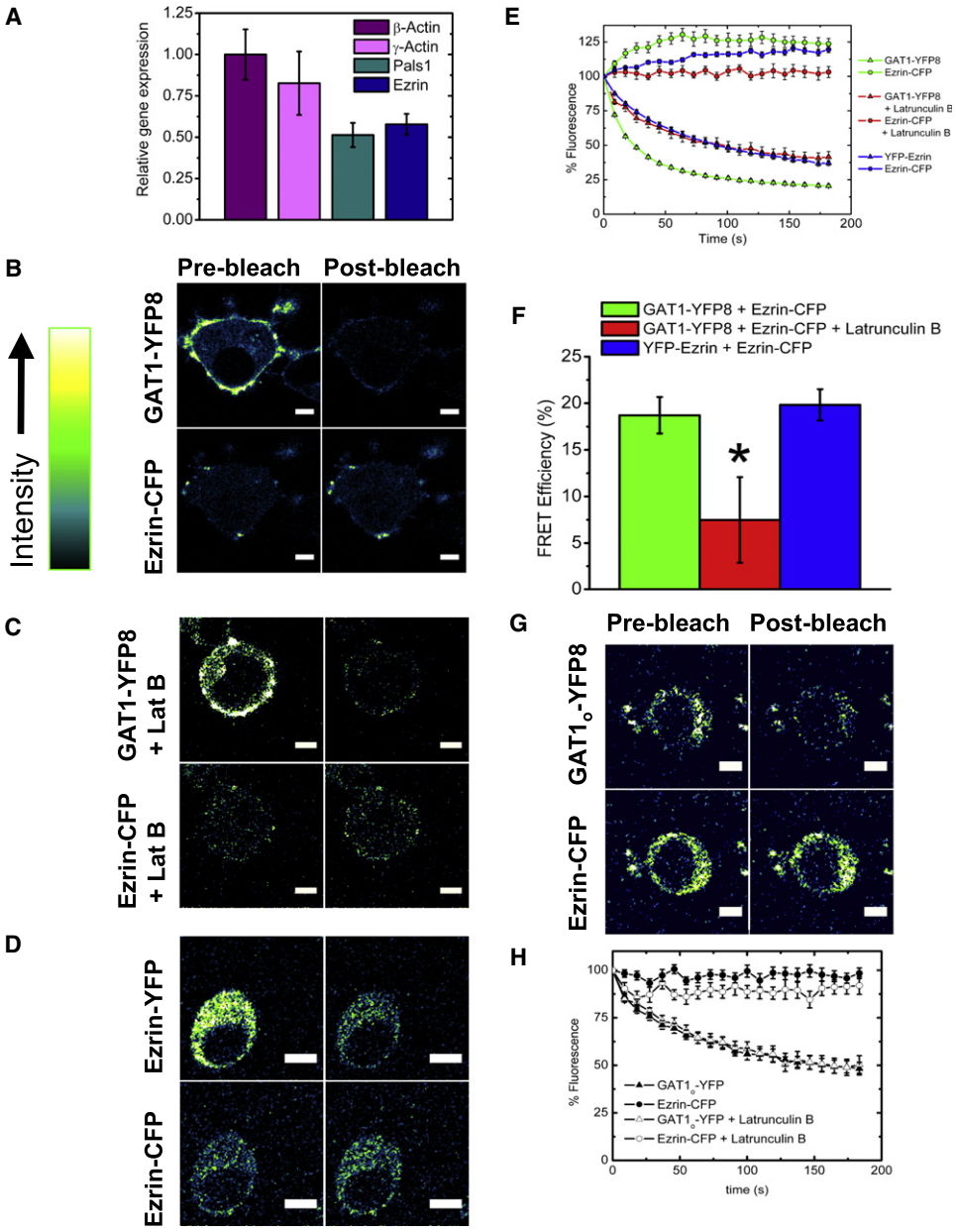

FIGURE 6 Determination of expression of ezrin and Pals1 in N2a cells by qRT-PCR, and an interaction between ezrin and GAT1-YFP8 by FRET. (*A*) mRNA levels of β-actin, γ-actin, ezrin, and Pals1, normalized to β-actin expression. One-step qRT-PCR shows that ezrin is expressed in N2a cells at levels similar to those of PDZ protein Pals1. (*B–D*) FRET results. Prebleaching and postbleaching images of respective CFP and YFP fused proteins. Images are processed using Image J software with the enhance-image plugin (Rasband, W.S.; US National Institutes of Health, Bethesda, MD). Scale bar, 5 μm. (*E*) GAT1-YFP8 and ezrin-CFP interact, as represented by the 25% $\pm$ 3% increase in ezrin-CFP fluorescence that accompanies photodestruction of GAT1-YFP8. The disruption of actin through the addition of 5 μm latrunculin B significantly decreased FRET between ezrin-CFP and GAT1-YFP8. As a positive control, FRET between YFP-ezrin and ezrin-CFP was performed, resulting in a 26% $\pm$ 3% increase in ezrin-CFP fluorescence that accompanied the photodestruction of YFP-ezrin. (*F*) FRET efficiency for ezrin-CFP/GAT1-YFP8 is 19% $\pm$ 2%, for ezrin-CFP/GAT1-YFP8 + latrunculin B it is 7% $\pm$ 5%, and for ezrin-CFP/YFP-ezrin it is 20% $\pm$ 2%. Values are represented as the mean $\pm$ SE of 23 replicates. Significance was determined by one-way analysis of variance with Tukey's post hoc test ($p < 0.05$). (*G*, *H*) As a negative control, experiments analogous to those in *B* were performed with $GAT1_0$-YFP. No detectable increase in ezrin-CFP fluorescence accompanied the photodestruction of $GAT1_0$-YFP. Scale bar, 5 μm.

expressed in our cell system. Through FRET, we also showed that GAT1 and ezrin participate in a latrunculin B-sensitive interactions. Furthermore, we observed no FRET between $GAT1_0$-YFP and ezrin-CFP, which further implicates the PDZ domain as essential to GAT1-actin interactions.

A direct link between GAT1 and ezrin is unlikely, because such direct linkage is typically stabilized via a triplet of positively charged residues in the juxta-membrane region (47,48). GAT1 does contain lysines in the N-terminus (K7, K26, K28, K33, K36, and K37). However, they are not adjacent, and this finding is not in accordance with the current understanding of direct ezrin interactions. Further research should elucidate whether these positive residues can participate in ezrin binding. However, our data indicate that the mobility of GAT1 is restricted by the actin cytoskeleton joined by a PDZ protein (for which Pals1 is a strong candidate molecule in many neurons) and ezrin.

The illustrations in Fig. 7 summarize these results. Fig. 7 *A* shows that an ezrin/PDZ complex can tether a membrane protein via the C-terminal PDZ-interacting domain (AYI). Disrupting actin abolishes the tetramolecular GAT1-PDZ protein-ezrin-actin complex, either by separating GAT1 from its PDZ protein (Fig. 7, *B1*), or by separating the ezrin-PDZ protein interaction (Fig. 7, *B2*). In either case, this frees GAT1, conferring higher mobility within the membrane. Finally, interrupting the endogenous C-terminal PDZ-interacting domain of GAT1 with a linker and a GFP

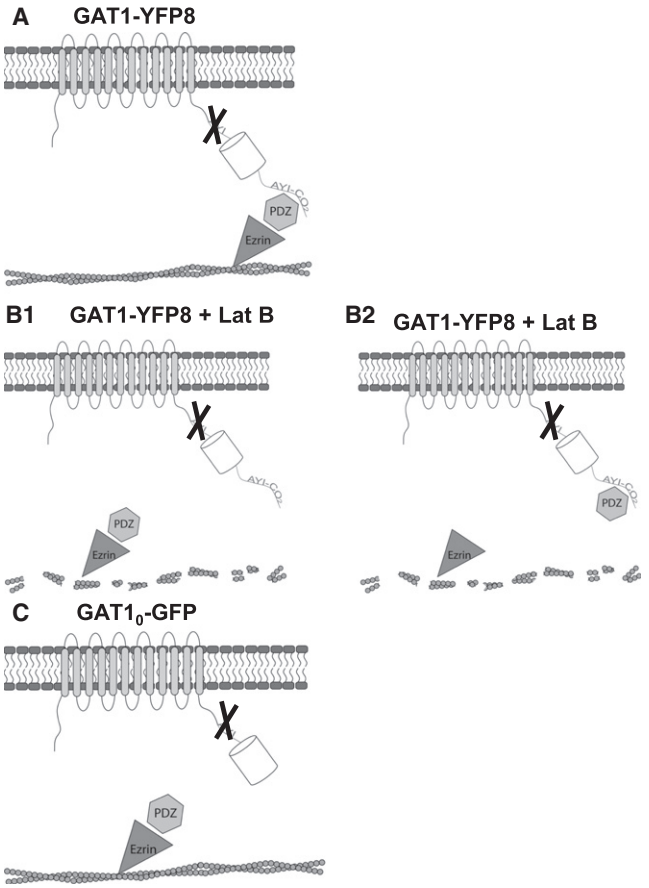

FIGURE 7 Schematic of GAT1 interactions with Pals1, ezrin, and actin. (*A*) Schematic of GAT1-YFP8 interaction with actin via ezrin and Pals1. The additional PDZ domain after YFP moiety restores the interaction between GAT1 and the PDZ protein. (*B*) The addition of 5 μM latrunculin B disrupts actin, and reduces the interaction between ezrin and GAT1 either by (*B1*) pulling away the GAT1-PDZ interaction, or (*B2*) reducing the interaction between ezrin and the PDZ protein. Altogether, this increases the mobility of GAT1 on the membrane. (*C*) GAT1$_0$-GFP, a GAT1 with a disrupted PDZ domain, is more mobile on the membrane, indicating that this domain may also stabilize the GAT1-ezrin-actin interactions.

moiety also increases the membrane mobility of GAT1 (Fig. 7 *C*). Additional members of the ezrin-radixin-moesin family of filamentous actin-binding proteins may also play a role in restricting GAT1 movements (34,49).

The $t_{1/2}$ values for the recovery of untreated GAT1-YFP8 are 3–10 times lower than the $t_{1/2}$ measured previously for GAT1 trafficking to and from the plasma membrane (9), supporting the idea that our measurements were not appreciably distorted by cytoplasmic/surface trafficking. However, the longest $t_{1/2}$ measured after actin disruption, ~1 min, may represent a component from cytoplasmic-surface interactions, which is further supported by the speckling that occurs after ~1 min in kymographic analysis of whole-cell photobleach (Fig. S2). Recent studies of aquaporin-2 revealed that actin reorganization may have a role in channel trafficking, possibly because aquaporin-2 itself regulates the local organization of actin (50). Further work should be performed to determine whether these increases in $t_{1/2}$ after latrunculin B and cytochalasin D treatment suggest a role for actin in GAT1 translocation, or whether these increases are attributable to an increased effective molecular weight of GAT1, by means of GAT1 retaining nonimmobilizing interactions with other molecules (27–29).

Microtubules play well-established roles in protein trafficking. Studies of the glycine receptor and GABA$_A$ receptor subunits suggest that microtubules may also affect receptor restriction to the plasma membrane via gephyrin scaffolding (13,32,49,51,52). Our results indicate that neither GAT1 immobilization nor its membrane diffusion depend on microtubules, after GAT1 has arrived at the plasma membrane.

Physiological significance of GAT1 movements in the membrane

One functional consequence of a disrupted actin cytoskeleton is increased GABA uptake, as evidenced by the several-fold increase in GABA uptake after actin depolymerization. Although Fig. 5 *B* also shows that depolymerizing actin does not significantly affect the mobile fraction of GAT1$_0$-GFP, Fig. 5 *C* shows that this treatment does increase the relatively small GABA uptake of GAT1$_0$-GFP, and by roughly the same ratio as for GAT1-YFP8. This increase in GABA uptake upon actin depolymerization suggests that actin plays an additional role in modulating transporter function. Further experiments beyond the scope of this study are required to determine whether the additional modulation occurs via a syntaxin isoform that interacts with both GAT1 and F-actin (53,54).

The GAT1 link to actin via ezrin may point to the role of this interaction in the pathophysiology and/or treatment of epilepsy. Although most studies of ezrin are focused on its role in epithelial structure, organization, and signaling, ezrin is also expressed in central nervous system neurons, and is increased, at both the mRNA and protein levels, in certain epilepsies. Ezrin is up-regulated in the hippocampus of patients with mesial temporal-lobe epilepsy (55,56). Likewise, in the lithium-pilocarpine-treated rat model of temporal-lobe epilepsy (57), ezrin is up-regulated within 48 h of seizure induction (58). Epilepsies associated with malformations of cortical development, such as focal cortical dysplasia (FCD$_{IIb}$ and FCD$_{IIa}$) and gangliogliomas, are also marked by neuronal ezrin accumulation (59). Although the role of ezrin up-regulation in seizure progression has not been formally identified, recent evidence points to the role of ezrin as a downstream target in the phosphoinositide 3-kinase pathway (59,60).

The identification of interactions between GAT1, ezrin, and actin, and our quantitative study using FRAP, contribute to a further understanding of how transporters are clustered, regulated, and confined on the cell surface. Because GAT1 is an important drug target in the treatment of epilepsy, continued research is needed to determine whether ezrin

up-regulation and GAT1 tethering play a neurotherapeutic role in epilepsy. Such protein interactions may lead to the discovery of additional therapeutics targeting GAT1 function (61–64).

SUPPORTING MATERIAL

Four figures are available at http://www.biophysj.org/biophysj/supplemental/S0006-3495(09)00408-1.

We thank Michael Quick and Elaine Bearer for valuable discussions.

This research was supported by grants from the National Institutes of Health (DA-09121, DK-60623, and NS-11756), by an American Heart Association Postdoctoral Fellowship to F.M., and by the Millard and Muriel Jacobs Genetics and Genomics Laboratory at the California Institute of Technology.

REFERENCES

1. Guastella, J., N. Nelson, H. Nelson, L. Czyzyk, S. Keynan, et al. 1990. Cloning and expression of a rat brain GABA transporter. *Science.* 249:1303–1306.
2. Minelli, A., N. C. Brecha, C. Karschin, S. DeBiasi, and F. Conti. 1995. GAT-1, a high-affinity GABA plasma membrane transporter, is localized to neurons and astroglia in the cerebral cortex. *J. Neurosci.* 15:7734–7746.
3. Morara, S., N. C. Brecha, W. Marcotti, L. Provini, and A. Rosina. 1996. Neuronal and glial localization of the GABA transporter GAT-1 in the cerebellar cortex. *Neuroreport.* 7:2993–2996.
4. Radian, R., and B. I. Kanner. 1983. Stoichiometry of sodium- and chloride-coupled γ-aminobutyric acid transport by synaptic plasma membrane vesicles isolated from rat brain. *Biochemistry.* 22:1236–1241.
5. Kavanaugh, M. P., J. L. Arriza, R. A. North, and S. G. Amara. 1992. Electrogenic uptake of γ-aminobutyric acid by a cloned transporter expressed in *Xenopus* oocytes. *J. Biol. Chem.* 267:22007–22009.
6. Mager, S., J. Naeve, M. Quick, C. Labarca, N. Davidson, et al. 1993. Steady states, charge movements, and rates for a cloned GABA transporter expressed in *Xenopus* oocytes. *Neuron.* 10:177–188.
7. Lester, H. A., S. Mager, M. W. Quick, and J. L. Corey. 1994. Permeation properties of neurotransmitter transporters. *Annu. Rev. Pharmacol. Toxicol.* 34:219–249.
8. Chiu, C. -S., K. Jensen, I. Sokolova, D. Wang, M. Li, et al. 2002. Number, density, and surface/cytoplasmic distribution of GABA transporters at presynaptic structures of knock-in mice carrying GABA transporter subtype 1-green fluorescent protein fusions. *J. Neurosci.* 22:10251–10266.
9. Wang, D., and M. W. Quick. 2005. Trafficking of the plasma membrane γ-aminobutyric acid transporter GAT1. Size and rates of an acutely recycling pool. *J. Biol. Chem.* 280:18703–18709.
10. Triller, A., and D. Choquet. 2005. Surface trafficking of receptors between synaptic and extrasynaptic membranes: and yet they do move!. *Trends Neurosci.* 28:133–139.
11. Ashby, M. C., S. R. Maier, A. Nishimune, and J. M. Henley. 2006. Lateral diffusion drives constitutive exchange of AMPA receptors at dendritic spines and is regulated by spine morphology. *J. Neurosci.* 26:7046–7055.
12. Richards, D. A., V. de Paola, P. Caroni, B. H. Gahwiler, and R. A. McKinney. 2004. AMPA-receptor activation regulates the diffusion of a membrane marker in parallel with dendritic spine motility in the mouse hippocampus. *J. Physiol. (Lond.).* 558:503–512.
13. Kirsch, J., and H. Betz. 1995. The postsynaptic localization of the glycine receptor-associated protein gephyrin is regulated by the cytoskeleton. *J. Neurosci.* 15:4148–4156.
14. Sun, F., M. J. Hug, C. M. Lewarchik, C. H. C. Yun, N. A. Bradbury, et al. 2000. E3KARP mediates the association of ezrin and protein kinase A with the cystic fibrosis transmembrane conductance regulator in airway cells. *J. Biol. Chem.* 275:29539–29546.
15. Zhang, J., R. E. Campbell, A. Y. Ting, and R. Y. Tsien. 2002. Creating new fluorescent probes for cell biology. *Nat. Rev. Mol. Cell Biol.* 3:906–918.
16. Geiser, M., R. Cebe, D. Drewello, and R. Schmitz. 2001. Integration of PCR fragments at any specific site within cloning vectors without the use of restriction enzymes and DNA ligase. *Biotechniques.* 31:88–90, 92.
17. Zhu, L., Y. Liu, and J. G. Forte. 2005. Ezrin oligomers are the membrane-bound dormant form in gastric parietal cells. *Am. J. Physiol. Cell Physiol.* 288:C1242–C1254.
18. An, S. J., and W. Almers. 2004. Tracking SNARE complex formation in live endocrine cells. *Science.* 306:1042–1046.
19. Lu, Y., S. Grady, M. J. Marks, M. Picciotto, J. -P. Changeux, et al. 1998. Pharmacological characterization of nicotinic receptor-stimulated GABA release from mouse brain synaptosomes. *J. Pharmacol. Exp. Ther.* 287:648–657.
20. De Brabander, M. J., R. M. L. Van de Velre, F. E. M. Aerts, M. Borgers, and P. A. J. Janssen. 1976. The effects of methyl [5-(2-thienylcarbonyl)-1H-benzimidazol-2-yl]carbamate, (R 17934; NSC 238159), a new synthetic antitumoral drug interfering with microtubules, on mammalian cells cultured in vitro. *Cancer Res.* 36:905–916.
21. Leach, R. N., J. C. Desai, and C. H. Orchard. 2005. Effect of cytoskeleton disruptors on L-type Ca channel distribution in rat ventricular myocytes. *Cell Calcium.* 38:515–526.
22. Vasquez, R. J., B. Howell, A. M. Yvon, P. Wadsworth, and L. Cassimeris. 1997. Nanomolar concentrations of nocodazole alter microtubule dynamic instability in vivo and in vitro. *Mol. Biol. Cell.* 8:973–985.
23. Ramamoorthy, S., E. Giovanetti, Y. Qian, and R. D. Blakely. 1998. Phosphorylation and regulation of antidepressant-sensitive serotonin transporters. *J. Biol. Chem.* 273:2458–2466.
24. Drenan, R. M., R. Nashmi, P. I. Imoukhuede, H. Just, S. McKinney, et al. 2007. Subcellular trafficking, pentameric assembly and subunit stoichiometry of neuronal nicotinic ACh receptors containing fluorescently-labeled α6 and β3 subunits. *Mol. Pharmacol.* 73:27–41.
25. Nashmi, R., M. E. Dickinson, S. McKinney, M. Jareb, C. Labarca, et al. 2003. Assembly of α4β2 nicotinic acetylcholine receptors assessed with functional fluorescently labeled subunits: effects of localization, trafficking, and nicotine-induced upregulation in clonal mammalian cells and in cultured midbrain neurons. *J. Neurosci.* 23:11554–11567.
26. Rabut, G., and J. Ellenberg. 2005. Photobleaching techniques to study mobility and molecular dyanmics of proteins in live cells: FRAP, iFRAP, and FLIP. *In* Live Cell Imaging: A Lab Manual. D. S. Robert and D. Goldman, editors. Cold Spring Harbor Laboratory Press, Cold Spring Harbor, NY, pp. 101–126.
27. Axelrod, D., D. E. Koppel, J. Schlessinger, E. Elson, and W. W. Webb. 1976. Mobility measurement by analysis of fluorescence photobleaching recovery kinetics. *Biophys. J.* 16:1055–1069.
28. Sprague, B. L., R. L. Pego, D. A. Stavreva, and J. G. McNally. 2004. Analysis of binding reactions by fluorescence recovery after photobleaching. *Biophys. J.* 86:3473–3495.
29. Sprague, B. L., and J. G. McNally. 2005. FRAP analysis of binding: proper and fitting. *Trends Cell Biol.* 15:84–91.
30. Lang, T., D. Bruns, D. Wenzel, D. Riedel, P. Holroyd, et al. 2001. SNAREs are concentrated in cholesterol-dependent clusters that define docking and fusion sites for exocytosis. *EMBO J.* 20:2202–2213.
31. Weiss, M. 2004. Challenges and artifacts in quantitative photobleaching experiments. *Traffic.* 5:662–671.
32. Chen, L., H. Wang, S. Vicini, and R. W. Olsen. 2000. The γ-aminobutyric acid type A ($GABA_A$) receptor-associated protein (GABARAP) promotes $GABA_A$ receptor clustering and modulates the channel kinetics. *Proc. Natl. Acad. Sci. USA.* 97:11557–11562.

33. Jacob, T. C., Y. D. Bogdanov, C. Magnus, R. S. Saliba, J. T. Kittler, et al. 2005. Gephyrin regulates the cell surface dynamics of synaptic $GABA_A$ receptors. *J. Neurosci.* 25:10469–10478.

34. Bretscher, A., K. Edwards, and R. G. Fehon. 2002. ERM proteins and merlin: integrators at the cell cortex. *Nat. Rev. Mol. Cell Biol.* 3:586–599.

35. Lopez-Corcuera, B., Q. R. Liu, S. Mandiyan, H. Nelson, and N. Nelson. 1992. Expression of a mouse brain cDNA encoding novel gamma-aminobutyric acid transporter. *J. Biol. Chem.* 267:17491–17493.

36. Bricker, J. L., S. Chu, and S. A. Kempson. 2003. Disruption of F-actin stimulates hypertonic activation of the BGT1 transporter in MDCK cells. *Am. J. Physiol. Renal Physiol.* 284:F930–F937.

37. Yun, C. H. C., G. Lamprecht, D. V. Forster, and A. Sidor. 1998. NHE3 kinase A regulatory protein E3KARP binds the epithelial brush border Na^+/H^+ exchanger NHE3 and the cytoskeletal protein ezrin. *J. Biol. Chem.* 273:25856–25863.

38. McHugh, E. M., W. Zhu, S. Milgram, and S. Mager. 2004. The GABA transporter GAT1 and the MAGUK protein Pals1: interaction, uptake modulation, and coexpression in the brain. *Mol. Cell. Neurosci.* 26:406–417.

39. Gary, R., and A. Bretscher. 1995. Ezrin self-association involves binding of an N-terminal domain to a normally masked C-terminal domain that includes the F-actin binding site. *Mol. Biol. Cell.* 6:1061–1075.

40. Bates, I. R., B. Hebert, Y. Luo, J. Liao, A. I. Bachir, et al. 2006. Membrane lateral diffusion and capture of CFTR within transient confinement zones. *Biophys. J.* 91:1046–1058.

41. Cha, B., A. Kenworthy, R. Murtazina, and M. Donowitz. 2004. The lateral mobility of NHE3 on the apical membrane of renal epithelial OK cells is limited by the PDZ domain proteins NHERF1/2, but is dependent on an intact actin cytoskeleton as determined by FRAP. *J. Cell Sci.* 117:3353–3365.

42. Haggie, P. M., B. A. Stanton, and A. S. Verkman. 2004. Increased diffusional mobility of CFTR at the plasma membrane after deletion of its C-terminal PDZ binding motif. *J. Biol. Chem.* 279:5494–5500.

43. Adkins, E. M., D. J. Samuvel, J. U. Fog, J. Eriksen, L. D. Jayanthi, et al. 2007. Membrane mobility and microdomain association of the dopamine transporter studied with fluorescence correlation spectroscopy and fluorescence recovery after photobleaching. *Biochemistry.* 46:10484–10497.

44. Torres, G. E., W. -D. Yao, A. R. Mohn, H. Quan, K. -M. Kim, et al. 2001. Functional interaction between monoamine plasma membrane transporters and the synaptic PDZ domain-containing protein PICK1. *Neuron.* 30:121–134.

45. Lamprecht, G., and U. Seidler. 2006. The emerging role of PDZ adapter proteins for regulation of intestinal ion transport. *Am. J. Physiol. Gastrointest. Liver Physiol.* 291:G766–G777.

46. Cao, X., X. Ding, Z. Guo, R. Zhou, F. Wang, et al. 2005. Pals1 specifies the localization of ezrin to the apical membrane of gastric parietal cells. *J. Biol. Chem.* 280:13584–13592.

47. Yonemura, S., M. Hirao, Y. Doi, N. Takahashi, T. Kondo, et al. 1998. Ezrin/radixin/moesin (ERM) proteins bind to a positively charged amino acid cluster in the juxta-membrane cytoplasmic domain of CD44, CD43, and ICAM-2. *J. Cell Biol.* 140:885–895.

48. Denker, S. P., D. C. Huang, J. Orlowski, H. Furthmayr, and D. L. Barber. 2000. Direct binding of the Na-H exchanger NHE1 to ERM proteins regulates the cortical cytoskeleton and cell shape independently of H^+ translocation. *Mol. Cell.* 6:1425–1436.

49. Kneussel, M., and S. Loebrich. 2007. Trafficking and synaptic anchoring of ionotropic inhibitory neurotransmitter receptors. *Biol. Cell.* 099:297–309.

50. Noda, Y., S. Horikawa, E. Kanda, M. Yamashita, H. Meng, et al. 2008. Reciprocal interaction with G-actin and tropomyosin is essential for aquaporin-2 trafficking. *J. Cell Biol.* 182:587–601.

51. Kirsch, J., D. Langosch, P. Prior, U. Z. Littauer, B. Schmitt, et al. 1991. The 93-kDa glycine receptor-associated protein binds to tubulin. *J. Biol. Chem.* 266:22242–22245.

52. Kneussel, M., and H. Betz. 2000. Receptors, gephyrin and gephyrin-associated proteins: novel insights into the assembly of inhibitory postsynaptic membrane specializations. *J. Physiol.* 525:1–9.

53. Deken, S. L., M. L. Beckman, L. Boos, and M. W. Quick. 2000. Transport rates of GABA transporters: regulation by the N-terminal domain and syntaxin 1A. *Nat. Neurosci.* 3:998–1003.

54. Jewell, J. L., W. Luo, E. Oh, Z. Wang, and D. C. Thurmond. 2008. filamentous actin regulates insulin exocytosis through direct interaction with syntaxin 4. *J. Biol. Chem.* 283:10716–10726.

55. Yang, J. W., T. Czech, M. Felizardo, C. Baumgartner, and G. Lubec. 2006. Aberrant expression of cytoskeleton proteins in hippocampus from patients with mesial temporal lobe epilepsy. *Amino Acids.* 30:477–493.

56. Lee, T. S., S. Mane, T. Eid, H. Zhao, A. Lin, et al. 2007. Gene expression in temporal lobe epilepsy is consistent with increased release of glutamate by astrocytes. *Mol. Med.* 13:1–13.

57. Andre, V., C. Dube, J. Francois, C. Leroy, M.-A. Rigoulot, et al. 2007. Pathogenesis and pharmacology of epilepsy in the lithium-pilocarpine model. *Epilepsia.* 48:41–47.

58. Greene, N. D., A. Bamidele, M. Choy, S. C. de Castro, R. Wait, et al. 2007. Proteome changes associated with hippocampal MRI abnormalities in the lithium pilocarpine-induced model of convulsive status epilepticus. *Proteomics.* 7:1336–1344.

59. Majores, M., V. Schick, G. Engels, J. Fassunke, C. Elger, et al. 2005. Mutational and immunohistochemical analysis of ezrin-, radixin-, moesin (ERM) molecules in epilepsy-associated glioneuronal lesions. *Acta Neuropathol. (Berl.).* 110:537–546.

60. Schick, V., M. Majores, A. Koch, C. E. Elger, J. Schramm, et al. 2007. Alterations of phosphatidylinositol 3-kinase pathway components in epilepsy-associated glioneuronal lesions. *Epilepsia.* 48:65–73.

61. Wu, Y., W. Wang, and G. B. Richerson. 2003. Vigabatrin induces tonic inhibition via GABA transporter reversal without increasing vesicular GABA release. *J. Neurophysiol.* 89:2021–2034.

62. Honmou, O., J. D. Kocsis, and G. B. Richerson. 1995. Gabapentin potentiates the conductance increase induced by nipecotic acid in CA1 pyramidal neurons in vitro. *Epilepsy Res.* 20:193–202.

63. Wu, Y., W. Wang, and G. B. Richerson. 2001. GABA transaminase inhibition induces spontaneous and enhances depolarization-evoked GABA efflux via reversal of the GABA transporter. *J. Neurosci.* 21:2630–2639.

64. Richerson, G. B., and Y. Wu. 2004. Role of the GABA transporter in epilepsy. *In* Advances in Experimental Medicine and Biology. D. K. Binder and H. E. Scharfman, editors. Kluwer Academic/Plenum Publishers, New York. 76–91.